Individual Scatterer Model Learning for Satellite Interferometry

Van De Kerkhof, Bas; Pankratius, Victor; Chang, Ling; Van Swol, Rob; Hanssen, Ramon F.

DOI
10.1109/TGRS.2019.2945370

Publication date
2020

Document Version
Accepted author manuscript

Published in
IEEE Transactions on Geoscience and Remote Sensing

Individual Scatterer Model Learning for Satellite Interferometry

Bas van de Kerkhof, Victor Pankratius, *Senior Member, IEEE*, Ling Chang, Rob van Swol, and Ramon F. Hanssen, *Senior Member, IEEE*

***Abstract*—Satellite-based persistent scatterer SAR interferometry facilitates the monitoring of deformations of the earth's surface as well as objects on it. A challenge in the data acquisition is the handling of large numbers of coherent radar scatterers. The behavior of each scatterer is time-dependent and is influenced by changes in deformation as well as other phenomena.**

Built environments are especially challenging, since scatterers may have different signal qualities and deformations may vary significantly among objects. Thus, the estimation of the actual deformation requires a functional model as well as a stochastic model, both of which are typically unknown per scatterer and observation. Here we present an approach that models the deformation behavior for each individual scatterer. Our technique is applied in a post-processing phase following the state-of-the-art interferometric processing of persistent scatterers. This addition significantly improves the interpretation of large data sets by separating the relevant phenomena classes more efficiently. It leverages more information than other methods from individual scatterers, which enhances the quality of the estimation and reduces residuals. Our evaluation shows that this technique can discriminate objects in terms of similar deformation characteristics that are independent of the specific spatial position and temporal complexity. Future applications analyzing large datasets collected by satellite radars will therefore drastically benefit from this new capability of extracting categorized types of time series behavior. This contribution will augment traditional spatial and temporal analysis and improve the quality of time-dependent deformation assessments.

***Index Terms*—Hypothesis Testing, InSAR, Machine Learning**

I. Introduction

SATELLITE radar (SAR) interferometry facilitates the detection and monitoring of deformations of the earth's surface or objects on it [1], [2], [3], [4], [5], [6], [7], [8], [9]. The core technique relies on interferometric phase observations of radar scatterers at different points in time. This data is used to estimate a set of parameters, such as surface displacement time series, geometric position, atmospheric delays of the radar signals, and integer phase ambiguities [10]. In a simple form that uses only two observations at different points in time, the deformation model can be parameterized as a displacement derived from the difference of two range measurements. However, the choice for modeling and parametrization can differ in practice for every scatterer, which is why the analysis of time series originating from many scatterers and observations can become challenging.

Conventionally, all points are assumed to have an initial steady-state displacement signal (linear velocity). This is a reasonable first-order assumption but excludes points with a significant non-stationary behavior that are typically found in built environments. This is why many techniques tend to mask out the built environment or perform various aggregations, thus missing out on the opportunity to gain insight on large swaths of satellite data.

New developments in high-resolution, wide-swath SAR systems with short revisit times have lead to an explosion of InSAR measurements. Datasets can now contain millions of scatterers, each of which can have many associated observations in time [11], [12], [13], [14], [15]. In urban environments, it is not uncommon that adjacent scatterers can exhibit completely different displacement signals, i.e., without any correlation in space or time. Thus, the analysis of such scatterers requires substantial effort that can be prohibitive for manual processing.

Coherent scatterers are strictly required for the estimation of functional model parameters describing time series of InSAR data. This implies that the phase noise for a particular scatterer should be low enough for essential processing steps, such as phase unwrapping, to be reliable [10]. The problem is that the estimation of coherence of a particular scatterer over time requires an a priori estimation of the unknown parameters in the observed phase. By imposing a simple steady-state model as a first order assessment of the coherence, scatterers that do not satisfy this condition will not be considered coherent and will be excluded from further evaluation. There are two coherence estimation methods that are typically used. The first one assumes spatial coherence and requires a spatially close connected or distributed group of scatterers to exhibit the same behavior [10], [16]. The second method assumes temporal coherence and requires temporally close measurements of the same scatterer to behave in a consistent way [7], [17], [18], [19].

Both the spatial and temporal coherence assumptions are sub-optimal for analyses involving similar objects that are spaced further apart than the respective spatial search window for coherence. For example, this situation is encountered with scattered buildings; another situation occurs when nearby

B. van de Kerkhof is with the Department of Geoscience and Remote Sensing, Delft University of Technology, Delft, The Netherlands (email: B.vandeKerkhof-1@tudelft.nl), and also with the Royal Netherlands Aerospace Centre (NLR), Amsterdam, The Netherlands and with the Massachusetts Institute of Technology, Cambridge, USA.

R. van Swol is with the Royal Netherlands Aerospace Centre (NLR), Amsterdam, The Netherlands.

R.F. Hanssen is with the Department of Geoscience and Remote Sensing, Delft University of Technology, Delft, The Netherlands.

V. Pankratius is with the Massachusetts Institute of Technology, Cambridge, MA, USA.

L. Chang is with the Faculty of Geo-Information Science and Earth Observation, University of Twente, The Netherlands.

scatterers express a totally different deformation behavior, when one scatters off a building and the other one off the ground nearby. Ideally, analysts would like to assume an object-based coherence that is categorical rather than spatial or temporal. Thus, a processing technique is required to detect and distinguish separate classes of scatterers with unique deformation behaviors. However, typical approaches in InSAR processing, [2], [3], [7], [20], [21], [22], [23], [24], [25], [26], and [27] are not equipped for this task.

To address this problem, we introduce the Individual Scatterer Model Learning method (ISML), a framework which attempts to model scatterers individually. ISML demonstrates that the use of machine learning algorithms can lead to significant improvements of parameter estimates and thus to a more accurate data interpretation. In Section II we describe the ISML method. Section III presents an in-depth case study on a dataset of TerraSAR-X data over the Netherlands. Section IV provides a conclusion and a discussion.

II. Methodology

The key idea of our approach is to group together time series that "behave" similarly over time. Machine learning algorithms allow for such analysis of large InSAR data volumes. Thus, a whole group of scatterers can be analyzed at once, thereby facilitating the model selection for each individual scatterer and obtaining enhanced estimates. To this end, we use (i) a dimensionality reduction technique [28], (ii) a clustering algorithm [29], and (iii) a functional model selection technique [30], [31].

A. Dimensionality reduction

t-Distributed Stochastic Neighbor Embedding (t-SNE) [28] is an unsupervised machine learning algorithm for dimensionality reduction. It is a variant of Stochastic Neighbor Embedding (SNE) as introduced by Hinton and Roweis in 2003 [32]. t-SNE converts a high-dimensional dataset into a low (e.g., two or three) dimensional representation by using the similarity between points in the high-dimensional dataset and comparing these with the similarity of the corresponding points in the low-dimensional representation. The aim of t-SNE is to minimize the mismatch between the similarity of points in the high-dimensional dataset and the similarity of the corresponding points in the low-dimensional representation.

Let x_i and x_j be points in the high-dimensional dataset and let y_i and y_j be the corresponding points in the low-dimensional representation respectively. The similarity of point x_i to point x_j equals the probability that x_i would choose x_j to be its neighbor according to a Gaussian distribution centered at x_i. The similarity of the corresponding points y_i and y_j equals the probability that y_i would choose y_j to be its neighbor according to a Student-t distribution centered at y_i. Now, the similarity of each point x_i in the high dimensional dataset to all other points x_j in this dataset can be compared to the similarity of the corresponding point y_i to all other points y_j in the low-dimensional representation. The mismatch between these similarities is minimized by using a cost function derived from the Kullback-Leibler divergence [33]. As a result, a large cost is introduced for representing nearby points in the high-dimensional dataset by largely separated points in the low-dimensional representation. In contrast, the cost of representing widely separated points in the high-dimensional dataset by nearby points in the low-dimensional representation is small, leading t-SNE to retain the local structure of the data. In order to minimize the cost function, the points in the low-dimensional representation move around in these dimensions accordingly during consecutive iterations using a gradient descent algorithm. For more detailed information regarding t-SNE see [28]. Results presented in [28] show that t-SNE is able to find a two or three dimensional representation of a high dimensional dataset in which the information-loss is minimized. This property of t-SNE makes it a suitable technique for our purpose of modeling each scatterer individually. It allows us to distinguish characteristic features of the data, both concerning the overall behavior over the entire domain as well as more detailed characteristic local features.

B. Clustering

The t-SNE method produces a point map that reveals useful information in a low-dimensional space. In our context, for instance, points that are close together represent similar time series, which suggests that their behavior might be subject to similar functional models. For this reason, applying a clustering technique will automatically identify groups of time series with similar physical behavior and free human analysts from the burden of checking each data set individually.

We employ the Density-Based Spatial Clustering of Applications with Noise algorithm (DBSCAN) [29] to identify clusters of time series with similar behavior. DBSCAN assigns points to a cluster when a given density is satisfied, and merges adjacent density components that are less than an ϵ measure apart. In contrast to other clustering algorithms like k-means, [34], or Gaussian Mixture Models, [35], DBSCAN does not require the number of clusters to be explicitly specified.

C. Functional model selection

Our ultimate objective is to select an optimal functional model for each individual scatterer, i.e., an optimal parameterization of the temporal displacement time series of the scatterer. In [31], MHT is based on a steady-state (constant velocity) null-hypothesis is tested using an overall model test (F-test). If rejected, it is tested against a library of alternative parameterizations using Baarda's B-method of testing [30]. This method is computationally intensive as it repeats the same sequence of testing independently for each scatterer against a large number of alternative hypotheses.

Although the time series representation of points in a cluster grouped by DBSCAN may actually belong to spatially dispersed scatterers, they are related through their similar time series behavior. In order to find a model representative for the general behavior of each cluster, we apply MHT on the average time series of each cluster. Next, we use this cluster representative model as null hypothesis while selecting the functional model for each point in the corresponding cluster using MHT. By using this cluster-dependent null hypothesis

in MHT instead of the steady-state model like the approach in [31], it is less likely to be rejected. This approach has two advantages. First, the fact that a cluster consists of a large number of points that exhibit similar behavior makes it more likely that we are not erroneously fitting a model to noise. Thus, the determined model may be more "physically realistic". Second, this approach significantly reduces the computational burden, because the number of alternative hypotheses to be tested is reduced.

D. Individual Scatterer Model Learning

The Individual Scatterer Model Learning (ISML) method combines the techniques from sections II-A, II-B and II-C to select the optimal functional model for each individual scatterer. ISML estimates the chosen parameters and the quality for those parameters.

Let D be a dataset containing persistent scatterer points, each having a displacement time series t_i, with $i = 1, \ldots, |D|$ and $|D|$ being the number of elements in D. Using t-SNE, the ISML method reduces the dimensionality of each time series from the number of measurements per time series to just two. This way, a map can be visualized to reveal structures in the data. DBSCAN clusters points whose associated time series representations exhibit similar behavior. A representative model is selected for each of the clusters using MHT. Next, an optimal functional model is selected for all points using MHT while leveraging their respective cluster-representative model. Finally, the parameters of the selected model are estimated, as well as their quality. The workflow of the ISML method is depicted in Figure 1, a formalized algorithm is outlined in **Algorithm 1**.

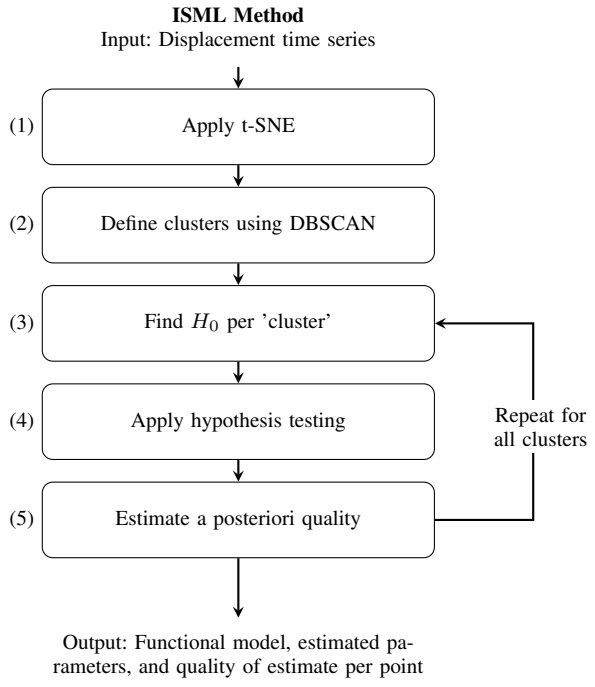

Fig. 1. Workflow of the ISML method.

Algorithm 1 ISML method

1: Let $D = \{t_1, \ldots, t_{|D|}\}$ be a dataset containing time series t_i, $i = 1, \ldots, |D|$. With $|D|$ being the number of elements in D.
2: Let m_j^i, $j = 1, \ldots, |t_i|$, $i = 1, \ldots, |D|$, be the j-th measurement of the i-th time series being the displacement in the line of sight direction. Note $t_i = \{m_1^i, \ldots, m_{|t_i|}^i\}$.
3: Apply t-SNE on dataset D resulting in a two-dimensional map $P = \{p_1, \ldots, p_{|D|}\}$. With p_i being the two-dimensional representation of the time series $t_i, \forall i = 1, \ldots, |D|$.
4: Set ϵ and N_{min} and apply DBSCAN on P resulting in a set of clusters $C = \{C_1, \ldots, C_{|C|}\}$, where $\exists k : p_i \in C_k, \forall i = 1, \ldots, |D|$.
5: **for** $k = 1$ **to** $|C|$ **do**
6: Calculate $\bar{T}_k$, being the average over $\forall t_i \in C_k$
7: Apply hypothesis testing on $\bar{T}_k$ using a steady-state null hypothesis resulting in H_0^k being the selected functional model.
8: **end for**
9: **for** $k = 1$ **to** $|D|$ **do**
10: Apply hypothesis on t_i using H_0^k with k such that $t_i \in C_k$ resulting in the functional model of t_i.
11: Calculate a posteriori sigma which is a quality metric for the selected functional model.
12: **end for**
13: **return** Functional model and quality of estimate per scatterer.

III. Case Study

We present an in-depth case study to demonstrate the capabilities of our method. The study uses a data set consisting of over one million scatterers with 95 observations each. This dataset was obtained by the TerraSAR-X satellite in StripMap mode in descending orbit between June 2013 and June 2016 and covers a part of the province Groningen, the Netherlands. We use the line-of-sight displacement measurements derived from unwrapped phase measurements processed using Persistent Scatterer Interferometry (PSI) processing, DePSI [23]. Contextual information (e.g., weather data and gas production data, when available) are used to interpret and validate the ISML method.

A. Power plant behavior

We applied steps 1–4 of the ISML method, **Algorithm 1**, on a regional subset of 7500 scatterers. Using t-SNE, the dimensionality of this subset is reduced from 95 to 2. Each time series is mapped to a single point in a 2D map. The clusters found by the DBSCAN algorithm are shown in different colors; for some clusters Figure 2 also depicts the corresponding time series. The computation time of this result, using Python 3.4 and a C++ Barnes-Hut t-SNE implementation, was approximately 2 minutes on a laptop computer with a 1.90 GHz processor.

Figure 2 illustrates that time series that are grouped in the same cluster indeed seem to behave in similar ways,

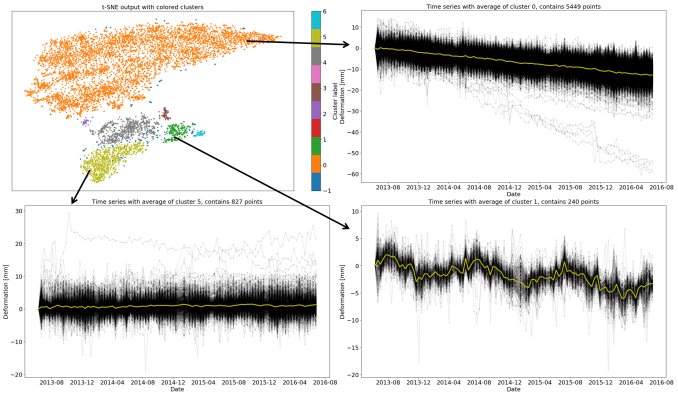

Fig. 2. Visualization of the combined output from t-SNE and DBSCAN for 7500 scatterers. Each point represents a time series of measurements. The cluster labels for each point are shown in different colors. Time series of line of sight displacement from different clusters are shown in black, whereas the average time series of a cluster is shown in yellow.

whereas different clusters capture other behaviors. Therefore, it is beneficial to derive a well-tuned functional model for the average time series behavior of each cluster, rather than deriving individual models for each time series. A default steady-state model will not capture the typical behavior per cluster. That approach would lead to larger residues between the model and the observations, thus resulting in an underestimation of the actual quality of the measurements.

Figure 3 illustrates an example of the spatial location of time series picked from distinctly different clusters. Figure 3A shows an aerial photo of the observed Eemscentrale power plant, with a top-down view in Figure 3B. The latter shows that all the points are in close proximity of each other on the same building. While the red points are located on part of the roof, the blue points are located on a structure which is on top of this roof. This structure is an air inlet system which acts as a filter unit to transfer air from outside to inside the power plant. This structure is mounted on a steel frame on top of the roof. The corresponding time series in figures 3C and 3D clearly demonstrate that the conventional assumption that all points behave in a similar way is invalid in this case. The red points show a linear subsiding behavior with a slope of $-1\,\mathrm{mm/year}$ while the blue points show the same linear behavior as well as a seasonal dependence with an amplitude of $4\,\mathrm{mm}$. The black line in figure 3D shows the daily average temperature of the closest weather station at 30 km distance. Visual comparison of this temperature behavior to the displacement behavior leads to the hypothesis that the displacement behavior of the blue points is temperature dependent.

Figure 3 illustrates the capability of ISML to distinguish different between types of scatterers in an automated way, regardless of their spatial location or temporal behavior.

B. Quality of estimated model

Following the functional model selection of ISML (steps 5–13 in **Algorithm 1**) we derive a functional model for all scatterers in cluster 1 as shown in Figure 2. All the blue points from Figure 3 are also included in this cluster. The cluster contains 240 points whose related time series are shown in the bottom right of Figure 2. The "average" time series is shown in yellow.

For the average time series of the cluster, using a linear steady-state functional model as the null hypothesis, an a priori sigma of 1 mm and a confidence level of 97.5%, leads to the null hypothesis being rejected. The a priori sigma is a measure of the expected quality of observations. The sustained alternative hypothesis is a periodic and temperature dependent model. All 240 points within the cluster were tested using this temperature dependent functional model, with a more conservative a priori sigma of 2 mm and a confidence level of 97.5%. Of the 240 points, 227 points sustained the null hypothesis and 13 points rejected the null hypothesis. Finally the quality of the selected model was calculated for each point. This a posteriori sigma is shown in Figure 4. The median value of the a posteriori sigma using ISML is 0.36 mm. For comparison, an alternative a posteriori sigma was calculated using the conventional hypothesis testing approach where a linear steady-state functional model is used as null hypothesis together with an a priori sigma of 2 mm and a confidence level of 97.5%, also shown in Figure 4. The distribution of the a posteriori sigma is wider, and the median value is 0.71 mm. Using this conventional approach, only 35 out of the 240 points sustained the temperature dependent model.

The results demonstrate that selecting the optimal functional model improves the interpretation and simultaneously increases the quality of the estimates. In this example, the ISML method performs two times better than the approach used in [31]. Indeed, the InSAR data is in fact much more precise than assumed before. Additionally, the computational burden of the hypothesis testing is reduced. The use of a cluster-dependent null hypothesis reduces the number of hypotheses to test, thereby reducing the computational time of the hypothesis testing in comparison to the approach following [31].

C. Eemscentrale validation

We check the plausibility of the temperature dependency of the time series in Figure 3D. Assuming this is the most likely functional model, we calculate the estimated deformation signal of the building's air inlet filter due to thermal expansion. These time series are also included in the time series in the bottom right of Figure 2. The air inlet filter rests on a steel frame, and we assume that the sinusoidal deformation as observed is due to thermal expansion of this frame. e subtract the mean deformation signal of the building on which the steel frame is mounted in order to remove this signal. Hence we subtract the mean of the red time series as shown in Figure 3C from the blue time series in Figure 3D. These corrected time series now show the deformation behavior of the air inlet system alone. The (linear) thermal expansion can be described as $\alpha_L = \frac{1}{L}\frac{dL}{dT}$, with α_L the linear expansion coefficient, L the length of the particular object and $\frac{dL}{dT}$ the rate of change of that linear dimension per unit change, [36]. Using a linear expansion coefficient of $17 \cdot 10^{-6} K^{-1}$, [36], and the average daily temperature as measured by the closest weather station, we can estimate the deformation signal in direction of the line of sight.

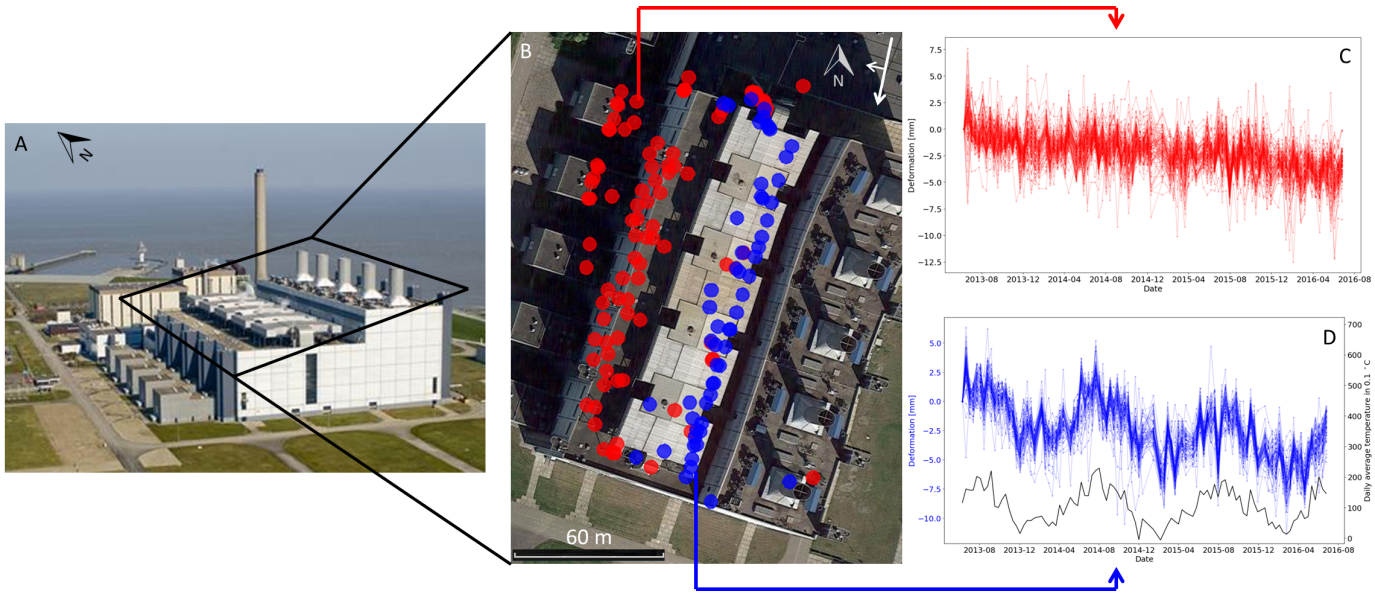

Fig. 3. A: Eemscentrale power plant building. B: Top-down aerial image. Points from different clusters from the t-SNE output in red and blue are located on the same building but show significantly different line of sight displacement behavior as shown in C and D. The black line in D shows the daily average temperature, which supports the hypothesis that the deformation behavior of the blue points is temperature-dependent.

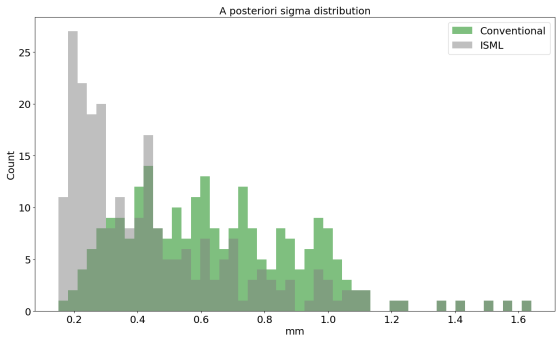

Fig. 4. Histograms of a posteriori sigmas using the conventional method and our ISML method. We can see an improvement in the estimation quality due to the smaller and narrower distribution of the a posteriori sigmas using the ISML method.

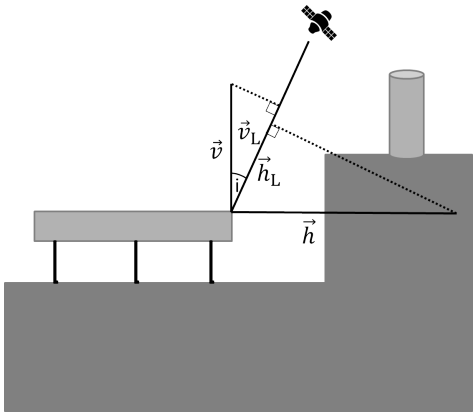

Fig. 5. Schematic drawing of the power plant in Figure 3. It shows the measurement geometry with $\vec{h}$ (horizontal displacement) and $\vec{v}$ (vertical displacement), $\vec{h}_L$ and $\vec{v}_L$ the corresponding projection of the displacement in the line of sight, and i as the incidence angle of the satellite.

We calculate the estimated deformation signal in horizontal and vertical direction as well as the corresponding line of sight displacement (see Figure 5). The corrected time series with their average are shown along with the estimated deformation signal in Figure 6. By visual inspection we can see that the average time series and the estimated deformation time series are very similar. They both show displacements between roughly $-2\,\mathrm{mm}$ and $2\,\mathrm{mm}$. This supports the plausibility of our hypothesis on the temperature dependence of the building's air inlet filter.

D. Gas storage field

Next, we applied the ISML method to a larger subset containing 250,000 scatterers each consisting of 95 observations in order to show the applicability of our approach to a larger dataset.

Among the clusters we found two clusters of which the time series show a periodic behavior. Figure 7B includes the average time series of both clusters (with different scales of the y-axis). The blue line shows a linear trend with a slope of $-3\,\mathrm{mm/year}$ and a periodic behavior with an amplitude between $2\,\mathrm{mm}$ and $4\,\mathrm{mm}$. The red line shows a linear trend with a slope of $-0.6\,\mathrm{mm/year}$ and a periodic behavior with an amplitude of $0.3\,\mathrm{mm}$. The spatial locations of a representative subset of the points within the two clusters are shown in Figure 7A. All the points in the blue cluster of the t-SNE output are also close in a spatial sense. It turns out that most of these points are located on the Norg gas storage field which is shown in Figure 7A.

The displacement behavior of the points in the blue cluster can be explained by the change in gas volume within the Norg gas storage field. When the volume increases or decreases

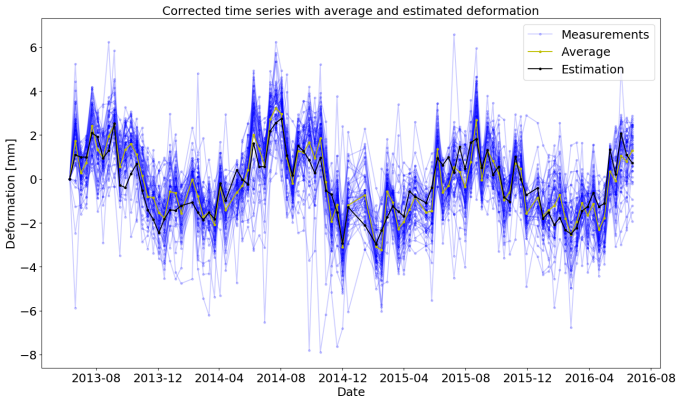

Fig. 6. Time series of Figure 3D corrected by subtracting the mean of the time series from Figure 3C. The resulting average time series is shown together with the estimated line of sight displacement signal due to thermal expansion.

the surface lifts or subsides, respectively. This phenomenon is observed 100 days after the actual change of volume, a delay in reacting to the gas injection, see Figure 7B. The gas volume change is shown as the black line in Figure 7C. Not all blue points are confined to the dimensions of the gas storage field (depicted in green in Figure 7A). This suggests that some points not far outside this region also behave in a similar fashion due to the volume change in the gas storage field. Thus, ISML automatically detected regions with scatterers that behaved in a similar fashion.

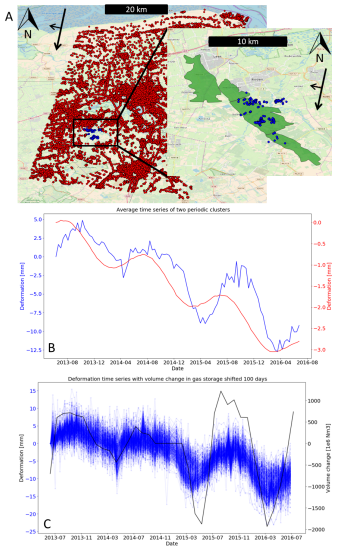

Fig. 7. A: Spatial location of clusters with periodic behavior. Scatterers in the blue cluster are located on the Norg gas storage field, which is shown in green. B: Average line of sight displacement time series of both clusters. C: All line of sight displacement time series of the blue cluster with gas volume change in the Norg field, shifted by 100 days

Next, we selected the functional model following steps 5–13 of ISML (**Algorithm 1**) for the points in the red cluster of Figure 7A. The periodic behavior of the time series in this cluster seems to have the same period as that of the time series in the bottom right of Figure 2 of which we hypothesize they are temperature dependent. However, the amplitude of this periodic behavior is smaller ($0.3\,\mathrm{mm}$) with respect to the other ($2\,\mathrm{mm}$).

We continue by applying hypothesis testing using a linear steady-state functional model as null hypothesis, with an a priori sigma of 1 mm and a confidence level of 97.5% on the average time series with the smaller amplitude. This cluster is shown in red in Figure 7A. The null hypothesis is sustained, thus supporting that a linear steady state model fits this average time series. However, when all 248,364 points within the cluster are tested using a temperature-dependent functional model as null hypothesis (with an a priori sigma of $2\,\mathrm{mm}$ and a confidence level of 97.5%) we find that 150,359 points sustain this (temperature dependent) null hypothesis, and the median of the a posteriori sigma equals $0.90\,\mathrm{mm}$. By comparison, calculating this value using the hypothesis testing approach where a linear steady-state functional model is used as null hypothesis together with an a priori sigma of $2\,\mathrm{mm}$ and a confidence level of 97.5%, we obtain a median value of the a posteriori sigma of $0.92\,\mathrm{mm}$. However, only 4,173 points sustained a temperature dependent model.

The results suggest that we do see an increase in quality using a temperature-dependent model as null hypothesis. However, its improvement is not as dramatic as for the example in Section III-B. Due to the small amplitude of the periodic signal, a steady state functional model does fit reasonably well. Nevertheless, more than 60% of all scatterers are now estimated with a more suitable functional model, which clearly shows the improvement on model selection using the ISML method.

E. Electricity posts

Another cluster from the output of the ISML method applied to the dataset as chosen in Section III-D reveals an interesting structure related to the corresponding spatial location of the scatterers (Figure 8A and B). The scatterers in the blue cluster are forming spatial linear structures. After further investigation of these linear structures, we concluded that these are in fact electricity posts (shown in Figure 8B and 8C).

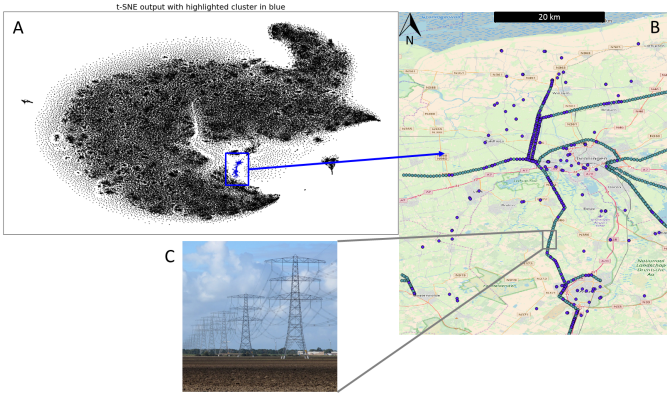

Fig. 8. A: t-SNE output. B: Blue highlighted cluster show scatterers on electricity posts with all electricity posts in the area of interests in gray. C: An example of a row of electricity posts.

This example demonstrates that scatterers may exhibit a similar behavior even when they are be spatially dispersed. This example contrasts the previous example of the gas

storage field where scatterers behave in a similar way and are spatially close (Figure 7). This kind of observations, spatially distributed scatterers showing similar behavior, are not captured using the conventional InSAR analysis approach due to the limited spatial search window. Therefore, being able to find such points is a significant novel result. It leads to a categorical notion of coherence rather than spatial or temporal, thereby augmenting traditional spatial and temporal analysis. Not all electricity posts are included in the cluster due to the fact that the time series are a superposition of the underlying physical mechanisms. Both the behavior of the electricity post as well as the behavior of the underlying ground are superposed in a single time series. The ground behaves differently for different spatial locations, so our method separates the electricity posts accordingly.

Results from the case study in Section III show the possibilities of the ISML method for increased information extraction from large InSAR datasets. The method provides a framework which leads to the categorization of scatterers. This categorization is based on clusters where each of the clusters has characteristic features. These characteristic features are not necessarily a result from the displacement signal only. They can also be other phenomena such as phase unwrapping errors that are consistent in time. These results demonstrate the wide applicability and versatility of the ISML method.

IV. Conclusion

Individual Scatterer Model Learning enhances information extraction from large InSAR datasets. It provides an unsupervised and automated way of selecting an optimal parameterization of the temporal displacement time series for each individual scatterer. Our method leads to significant improvements in data interpretation, parameterization, as well as to an increase in the quality of the estimated parameters. Thereby it improves the quality of time-dependent deformation assessments and generates new geophysical insights. Traditional analyses can now be performed in a less compute-intensive manner by analyzing groups of scatterers with similar behavior all at once rather than one-by-one. In addition, the proposed method is independent of the spatial location and temporal properties of the data and can be generally applied to all kinds if InSAR time series. Leveraging information in new ways also suggests that collected InSAR data seems to be more precise than previously assumed. Thus it opens up new possibilities in performing a categorical analysis that augments traditional spatial and temporal analyses. We expect that our methodology will contribute to an easier handling of Big Data in the satellite radar community, thereby improving information extraction from large satellite radar datasets.

Acknowledgment

Victor Pankratius would like to acknowledge support from NASA AISTNNX15AG84G and NSF ACI-1442997.

References

[1] D. Massonnet, M. Rossi, C. Carmona, F. Adragna, G. Peltzer, K. Feigl, and T. Rabaute, "The displacement field of the landers earthquake mapped by radar interferometry," *Nature*, vol. 364, no. 6433, p. 138, 1993.

[2] A. Ferretti, C. Prati, and F. Rocca, "Permanent scatterers in sar interferometry," *IEEE Transactions on geoscience and remote sensing*, vol. 39, no. 1, pp. 8–20, 2001.

[3] P. Berardino, G. Fornaro, R. Lanari, and E. Sansosti, "A new algorithm for surface deformation monitoring based on small baseline differential sar interferograms," *IEEE Transactions on Geoscience and Remote Sensing*, vol. 40, no. 11, pp. 2375–2383, 2002.

[4] T. J. Wright, B. Parsons, P. C. England, and E. J. Fielding, "Insar observations of low slip rates on the major faults of western tibet," *Science*, vol. 305, no. 5681, pp. 236–239, 2004.

[5] A. Hooper, H. Zebker, P. Segall, and B. Kampes, "A new method for measuring deformation on volcanoes and other natural terrains using insar persistent scatterers," *Geophysical research letters*, vol. 31, no. 23, 2004.

[6] Z. Perski, R. Hanssen, A. Wojcik, and T. Wojciechowski, "Insar analyses of terrain deformation near the wieliczka salt mine, poland," *Engineering Geology*, vol. 106, no. 1-2, pp. 58–67, 2009.

[7] A. Ferretti, A. Fumagalli, F. Novali, C. Prati, F. Rocca, and A. Rucci, "A new algorithm for processing interferometric data-stacks: Squeesar," *IEEE Transactions on Geoscience and Remote Sensing*, vol. 49, no. 9, pp. 3460–3470, 2011.

[8] L. Chang and R. F. Hanssen, "Detection of cavity migration and sinkhole risk using radar interferometric time series," *Remote Sensing of Environment*, vol. 147, pp. 56–64, 2014.

[9] T. Wang, Q. Shi, M. Nikkhoo, S. Wei, S. Barbot, D. Dreger, R. Bürgmann, M. Motagh, and Q.-F. Chen, "The rise, collapse, and compaction of mt. mantap from the 3 september 2017 north korean nuclear test," *Science*, p. eaar7230, 2018.

[10] R. F. Hanssen, *Radar Interferometry: Data Interpretation and Error Analysis*. Dordrecht: Kluwer Academic Publishers, 2001.

[11] M. Eineder, N. Adam, R. Bamler, N. Yague-Martinez, and H. Breit, "Spaceborne spotlight sar interferometry with terrasar-x," *IEEE Transactions on Geoscience and Remote Sensing*, vol. 47, no. 5, pp. 1524–1535, 2009.

[12] R. Werninghaus and S. Buckreuss, "The terrasar-x mission and system design," *IEEE Transactions on Geoscience and Remote Sensing*, vol. 48, no. 2, pp. 606–614, 2010.

[13] M. Eineder, C. Minet, P. Steigenberger, X. Cong, and T. Fritz, "Imaging geodesy—toward centimeter-level ranging accuracy with terrasar-x," *IEEE Transactions on Geoscience and Remote Sensing*, vol. 49, no. 2, pp. 661–671, 2011.

[14] R. Torres, P. Snoeij, D. Geudtner, D. Bibby, M. Davidson, E. Attema, P. Potin, B. Rommen, N. Floury, M. Brown *et al.*, "Gmes sentinel-1 mission," *Remote Sensing of Environment*, vol. 120, pp. 9–24, 2012.

[15] A. Rucci, A. Ferretti, A. M. Guarnieri, and F. Rocca, "Sentinel 1 sar interferometry applications: The outlook for sub millimeter measurements," *Remote Sensing of Environment*, vol. 120, pp. 156–163, 2012.

[16] A. Hooper, P. Segall, and H. Zebker, "Persistent scatterer interferometric synthetic aperture radar for crustal deformation analysis, with application to volcán alcedo, galápagos," *Journal of Geophysical Research: Solid Earth*, vol. 112, no. B7, 2007.

[17] B. M. Kampes, *Radar interferometry*. Springer, 2006.

[18] F. J. van Leijen, *Persistent Scatterer Interferometry based on geodetic estimation theory*. Netherlands Geodetic Commission, 2014, no. 86.

[19] J. J. Sousa, A. J. Hooper, R. F. Hanssen, L. C. Bastos, and A. M. Ruiz, "Persistent scatterer insar: A comparison of methodologies based on a model of temporal deformation vs. spatial correlation selection criteria," *Remote Sensing of Environment*, vol. 115, no. 10, pp. 2652–2663, 2011.

[20] O. Mora, R. Lanari, J. J. Mallorqui, P. Bernadino, and E. Sansosti, "A new algorithm for monitoring localized deformation phenomena based on small baseline differential SAR interferograms," in *igarss02*, 2002.

[21] O. Mora, J. J. Mallorqui, and A. Broquetas, "Linear and nonlinear terrain deformation maps from a reduced set of interferometric SAR images," *TGARS*, vol. 41, no. 10, pp. 2243–2253, 2003.

[22] R. Lanari, O. Mora, M. Manunta, J. J. Mallorquí, P. Berardino, and U. Sansosti, "A small-baseline approach for investigating deformations on full-resolution differential SAR interferograms," *TGARS*, vol. 42, no. 7, pp. 1377–1386, 2004.

[23] B. M. Kampes, R. F. Hanssen, and Z. Perski, "Radar interferometry with public domain tools," in *Proceedings of FRINGE*, vol. 3, 2003.

[24] A. J. Hooper, "Persistent scatter radar interferometry for crustal deformation studies and modeling of volcanic deformation," *JOURNAL OF GEOPHYSICAL RESEARCH*, 2006.

[25] *Delft Object-oriented Radar Interferometric Software (DORIS), User's manual and technical documentation*, Delft Institute of Earth Observation and Space Systems (DEOS), Delft University of Technology, Delft, The Netherlands, 1998.

[26] K. Goel and N. Adam, "A Distributed Scatterer Interferometry Approach for Precision Monitoring of Known Surface Deformation Phenomena," *IEEE Transactions on Geoscience and Remote Sensing, Geoscience and Remote Sensing*, vol. 52, no. 9, pp. 5454–5454–5468, sep 2014.

[27] S. Samsonov and N. d'Oreye, "Multidimensional time-series analysis of ground deformation from multiple insar data sets applied to virunga volcanic province," *Geophysical Journal International*, vol. 191, no. 3, pp. 1095–1108, 2012.

[28] L. van der Maaten and G. Hinton, "Visualizing data using t-SNE," *Journal of Machine Learning Research*, vol. 9, no. Nov, pp. 2579–2605, 2008. [Online]. Available: http://www.jmlr.org/papers/v9/vandermaaten08a.html

[29] M. Ester, H.-P. Kriegel, J. Sander, and X. Xu, "A density-based algorithm for discovering clusters a density-based algorithm for discovering clusters in large spatial databases with noise," in *Proceedings of the Second International Conference on Knowledge Discovery and Data Mining*, ser. KDD'96. AAAI Press, 1996, pp. 226–231. [Online]. Available: http://dl.acm.org/citation.cfm?id=3001460.3001507

[30] W. Baarda, "A testing procedure for use in geodetic networks." *Netherlands Geodetic Commission, Publications on Geodesy*, vol. 2, no. 5, 1968.

[31] L. Chang and R. F. Hanssen, "A probabilistic approach for insar time-series postprocessing," *IEEE Transactions on Geoscience and Remote Sensing*, vol. 54, no. 1, pp. 421–430, Jan 2016.

[32] G. E. Hinton and S. T. Roweis, "Stochastic neighbor embedding," in *Advances in neural information processing systems*, 2003, pp. 857–864.

[33] S. Kullback and R. A. Leibler, "On information and sufficiency," *The annals of mathematical statistics*, vol. 22, no. 1, pp. 79–86, 1951.

[34] J. Macqueen, "SOME METHODS FOR CLASSIFICATION AND ANALYSIS OF MULTIVARIATE OBSERVATIONS," *MULTIVARIATE OBSERVATIONS*, p. 17, 1967.

[35] G. J. McLachlan and K. E. Basford, "Mixture models. Inference and applications to clustering," *Journal of the Royal Statistical Society*, 1988.

[36] F. Cverna, *ASM Ready Reference - Thermal Properties of Metals*. ASM International, 2002. [Online]. Available: https://app.knovel.com/hotlink/toc/id:kpASMRRTP1/asm-ready-reference-thermal/asm-ready-reference-thermal

Bas van de Kerkhof recieved the M.Sc. degree in Applied Mathematics from the University of Twente in 2014. He is now pursuing a Ph.D. degree in Geoscience and Remote Sensing at Delft University of Technology where he works on information extraction from InSAR data using machine learning techniques. He is also a R&D Engineer at the Royal Netherlands Aerospace Centre (NLR) in Amsterdam. Here he works on various topics including data analysis and automated information extraction from satellite sensor data.

Victor Pankratius received a Dr.rer.pol. with distinction from the University of Karlsruhe, Germany, in 2007, and a Habilitation in Computer Science from the Karlsruhe Institute of Technology, Germany, in 2012. Currently he leads the Data Science for Astro-&Geoinformatics group at MIT. Victor's research spans multiple departments, and he serves as principal investigator in NASA and NSF projects. He is passionate about advancing data science through novel computational methods involving domain-aware artificial intelligence, scalable parallel computing, and software engineering for artificial intelligence systems. Contact him at victorpankratius.com

Ling Chang received the M.S.E. degree in geodesy and survey engineering from Tongji University, Shanghai, China, in 2010, and the Ph.D. degree in geodetic engineering from the Delft University of Technology, Delft, The Netherlands, 2015. Since 2018, she has been an Assistant Professor of microwave remote sensing with the ITC, University of Twente, Enschede, The Netherlands. Her current research interests include statistical hypothesis testing, time series modeling, and change detection, using satellite-borne remote sensing technology

Rob van Swol received the M.Sc. degree in Experimental Physics and the Ph.D. degree in Mathematics and Sciences (High Energy Physics) from the University of Amsterdam, The Netherlands in 1980 and 1985, respectively. Rob is senior scientist at the Royal Netherlands Aerospace Centre (NLR) in Amsterdam where he works in the field of earth observation and geomatics. He has a long-standing experience with many aspects of acquiring, processing and interpretation of data collected by optical and radar systems. Currently, his main activities focus on the application of novel computational techniques and computing infrastructures for automated processing and information extraction from satellite sensor data.

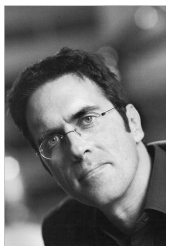

Ramon Hanssen (M'04–SM'15) received the M.Sc. degree in geodetic engineering and the Ph.D. (cum laude) degree in geodetic engineering from the Delft University of Technology, Delft, The Netherlands, in 1993 and 2001, respectively. He was with the International Institute for Aerospace Survey and Earth Science, Stuttgart University; the German Aerospace Center (DLR); Stanford University (Fulbright Fellow); and the Scripps Institution of Oceanography where he worked on microwave remote sensing, radar interferometry, signal processing, and geophysical application development. Since 2008, he has been an Antoni van Leeuwenhoek Professor in earth observation with the Delft University of Technology. He is the author of a textbook on radar interferometry.